Journal of Materials Chemistry A

Accepted Manuscript

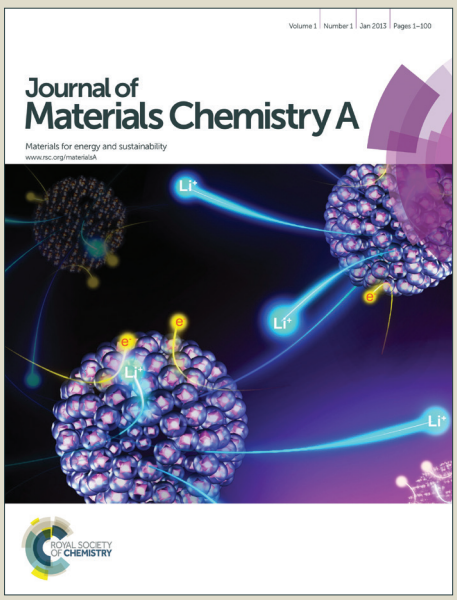

ROYAL SOCIETY OF CHEMISTRY

www.rsc.org/materialsA

Cite this: DOI: 10.1039/c0xx00000x

www.rsc.org/xxxxxx

ARTICLE TYPE

Probing the unexpected behavior of AuNPs immigrating through the nanofibers: A new strategy for the fabrication of carbon nanofibers-noble metal nanocrystals hybrid nanostructures

Han Zhu[a], MingLiang Du*[a,b], Ming Zhang[a,b], MeiLing Zou[a], TingTing Yang[a], LiNa Wang[b], JuMing Yao[a,b], BaoChun Guo[c]

Received (in XXX, XXX) Xth XXXXXXXXX 20XX, Accepted Xth XXXXXXXXX 20XX
DOI: 10.1039/b000000x

Intimate relation of electrochemical sensors with high sensitivity and reliability has stimulated intensive researches on developing versatile materials with excellent electrocatalytic activity. Here, we reported a novel strategy for the design of novel nanostructure-based electrochemical biosensors originating from an unexpected behavior of Au nanoparticles (AuNPs) embedded in the internal polyacrylonitrile nanofibers (Au-PANFs), which can emigrate to the external surfaces of the carbon nanofibers (Au-CNFs) during the graphitization process. Small and uniform AuNPs embedded in PANFs were synthesized via a combination of electrospinning and *in situ* reduction. With the conversion from the amorphous structures of PANFs to graphene layered structures of CNFs, the AuNPs can emigrate from the internal PANFs to the external surfaces of CNFs. The emigrations of AuNPs through the nanofiber matrix are strongly depended on the graphitization temperature and heating rates. Three different heating rates at 2, 5, 10 ^{o}C/min and graphitization temperatures at 600, 800, 1000 ^{o}C were performed to investigate the emigrations and the exposed density of AuNPs on the CNFs. These novel nanomaterials were constructed as a nonenzymatic H_2O_2 electrochemical sensor and the sensors based on Au-CNFs with increased density of exposed AuNPs exhibit significant promoted electrochemical activity. The Au-CNFs (1000 ^{o}C, 2 ^{o}C/min) with high exposed density and small sizes of AuNPs possess higher specific surface area and active sites, leading to the relative higher electrocatalytic activity. The present investigations provide a general route for the fabrication of nanostructures for novel electrochemical sensors, energy storage devices and so on.

Introduction

Over the last two decades, the development of new electronic devices for wide applications in the sensitive detection of clinical, environmental, and food safety is currently an area of intensive research.[1-2] In this context, materials with dimensions at the nanoscale appear highly promising due to their exciting physical and chemical properties for the selective detection with low limits. Nanomaterials-based sensors exhibit extremely high surface area to volume ratio, which can increase the number of binding sites available for biological recognition element immobilization.[3-6] In addition, the unitization of nanomaterials usually leads to faster mass transfer rates, resulting in lower limits of detection and faster analyte detection rates than those seen in conventional sensors.[5,7-8]

Large amounts of nanomaterials, such as noble metal NPs, carbon nanotubes (CNTs) and graphene, are employed to construct the electrochemical biosensors.[9-14] Electrochemical detection of biomolecules using nanomaterials can often achieve high sensitivity because nanomaterials are extremely sensitive to electronic perturbations in the surrounding environment. Considerable efforts were devoted to novel nanomaterials to coordinate mass- and charge-transport and electron-transfer kinetics for realizing simultaneous minimization of primary resistances in biosensing: electrochemical reaction occurring at electrolyte/electrode interface, mass transport of analyte in electrolyte and electrode, and the electron conduction in electrode and current collector.[1,12-14]

Carbonaceous materials, such as CNTs and graphene, are of enormous interest, mainly due to their superior electrocatalytic activity for various chemical and biological systems.[15-17] The control of heterogeneous electron-transfer kinetics through judicious design and structural manipulation of advanced carbon materials is of importance in the fabrication of many electrochemical devices such as biosensors.[8,15] Several groups

[a] *Department of Materials Engineering, College of Materials and Textile, Zhejiang Sci-Tech University, Hangzhou 310018, P. R. China*
[b] *Key Laboratory of Advanced Textile Materials and Manufacturing Technology, Zhejiang Sci-Tech University, Ministry of Education, Hangzhou 310018, P. R. China*
c Department of Polymer Materials and Engineering, South China University of Technology, Guangzhou 510640, P. R. China
Tel: 86-571-86843255; E-mail: du@zstu.edu.cn
Electronic Supplementary Information (ESI) available: See DOI:

have demonstrated the successful fabrication of sensitive biosensors using CNTs and graphene.[16-19] These sensors utilize the fast mass transfer and large surface areas provided by the carbonaceous nanomaterials. Myung *et al.* have reported the construction of graphene-encapsulated nanoparticle-based biosensor for the selective detection of cancer biomarkers.[9] Chen *et al.* have fabricated the CNTs-based electrochemical devices for the electronic sensing of protein.[10]

Up to date, one-dimensional electrospun carbon nanofibers (CNFs) have been widely used as ideal electron pathways because of their intriguing chemical and physical properties such as good conductivity (ρ = (3-7) × 10^{-3} Ω cm).[17,20-23] Electrospinning is a highly versatile method to produce nanofibers of various polymers with diameters ranged from a few tens of nanometers to a few micrometers in different forms such as nonwoven mats, yarns, etc.[21-23] It is a relatively simple and low-cost strategy to produce continuous nanofibers from polymer solutions or melts. CNFs synthesized via electrospinning and subsequent graphitization had attracted attention mainly because their structures and properties can be easily adjusted by changing processing conditions. Similar with other carbonaceous materials, electrospun CNFs are mostly used in the electrochemical applications related to the energy storage devices including lithium-ion batteries, supercapacitors, and fuel cells.[24-27] Only a few researches focus on the electrochemical sensor applications of the electrospun CNFs. In addition, the electrocatalytic activities of CNFs are often adjusted through the utilization of additional active component, such as loading or deposition of metal NPs onto the nanofibers.

Combining different materials with precise control of their interface at the nanoscale would lead to significantly enhanced properties. Noble metal nanostructures, especially Au nanostructures, have proven to be the most intriguing platforms suitable for a broad spectrum of bioapplications due to their bioinertness and biocompatibility, relatively simple and facile synthetic control and bioconjugation.[1,8,15] Recent years have witnessed tremendous efforts devoted to the design and synthesis of Au nanostructures in the application of electrochemical biosensors.[1,16] Au nanostructure-based electrochemical biosensors are extremely sensitive to the sizes, shapes and dispersion of Au nanostructures.[15,18,28-29] Recently, our group have reported the designs of noble metal nanostructures decorated one-dimension organic nanofibers, employing as the electrochemical biosensors for the detection of H_2O_2, glucose and glutathione.[30-33] Small sizes of Au nanocrystals usually can dramatically influence their physical and chemical properties arising from their large surface-area-to-volume ratio and the spatial confinement of electrons, phonons, and electric fields in and around these particles.[30-31] These novel nanocrystal-nanofiber hybrid architectures exhibit high surface area and strong electrochemical activities, leading to advanced materials for electrochemical sensors, nanoelectronics, energy storage devices and catalysts.

Unlike organic nanofibers, the structure of CNFs is lack of functional groups and consequently relatively chemical inert. Common strategies to decorate the CNFs with nanocrystals include surface treatments by ultrasonication and acid-assisted oxidation, vapor deposition and solution growth.[34-36] Hermans *et al.* have reported that CNTs and CNFs functionalized with HNO_3 can produce surface carboxyl groups, serving as anchoring points for the grafting of PdNPs.[37] Kvande *et al.* have synthesized the PdNPs functionalized CNF composites through a two-step chemical vapor deposition of Pd(allyl)(Cp).[38] However, because of complex interfacial reactions involved and more demanding process conditions imposed, the size and distribution control of nanocrystals on CNFs becomes thorny problems. How to synthesize excellent electrochemical sensors based on CNFs incorporated with small and uniform nanocrystals still remains huge challenges.

Recently, Yang *et al.* have reported an approach to prepare CNFs decorated with SnO_2 nanocrystals by combining the PANFs and stannous chloride salts solution.[39] After the carbonization by Ar/H_2O atmosphere, the SnO_2-NPs were formed on the surfaces of the CNFs. Similarly, Hou *et al.* prepared the PANFs mixed with Fe(acetylacetonate)$_3$ to synthesize CNFs/Fe nanocomposites and the FeNPs immobilized on the CNFs can serve as the catalysts for the growth of CNTs.[40]

Unlike the above common strategies and new raised thermal decomposition approaches, we proposed a new strategy and synthesized a new system, CNFs-Au nanostructures. In the procedure, accompanied with the conversion from PANFs to CNFs, the nanostructure of CNFs-Au and can be assembled and tailored by the emigration of AuNPs in PANFs to the outside of CNFs during the graphitization process. Our previous work has reported a green and facile approach for the synthesis of small and uniform AuNPs embedded in the interior of the PANFs via a combination of electrospinning and *in situ* reduction.[41-42] Note that intriguing phenomena can be observed during the graphitization process. With the conversion from the amorphous structures of PANFs to graphene layered structures of CNFs, the initial AuNPs emigrate from the internal PANFs to the external CNFs. The emigrations of AuNPs through the nanofiber matrix are strong depended on the graphitization temperature and heating rates. We performed three different heating rates at 2, 5, 10 °C/min and graphitization temperatures at 600, 800, 1000 °C, respectively, to investigate the emigrations and the exposed density of AuNPs on the CNFs. The conversion from embedded AuNPs to exposed AuNPs attached to the external surfaces of CNFs is explained by an atom diffusion mechanism. In addition, we also investigate the conversion in the chemical structures from -C≡N structure to -C=C-C=N structure during the graphitization process. Similar phenomena can be obtained by Pt-CNFs hybrid nanostructures, indicating that this new strategy will provide a general approach for the fabrication of CNFs-noble metal nanostructures. These novel nanomaterials were constructed as a nonenzymatic H_2O_2 electrochemical sensor. The electrochemical sensors based on Au-CNFs with increased density of exposed AuNPs exhibit significantly promoted electrochemical activity with increased density of exposed AuNPs. The Au-CNFs with high density of exposed AuNPs possess higher specific surface area and active sites. It means that more AuNPs will take part in the reactions, leading to the relative higher electrocatalytic activity. The sensors show lower detection limit and wider responding range, indicating that the fabricated sensor could be potentially used for monitoring the concentration of H_2O_2 without any enzyme.

Experiment section

Materials and methods

Materials

Chloroauric acid ($HAuCl_4 \cdot 4H_2O$, 99.9%), hydrogen per-oxide (30 %), hydroquinone (HQ), phosphate buffered saline (PBS) and dimethyl formamide (DMF, 99.5%) were commercially available from Shanghai Civi Chemical Technology Co., Ltd. Polyacrylonitrile (PAN, Mw≈1.4×10^5, copolymerized with 10 wt% methyl acrylate) was manufactured by Sinopec Shanghai Petrochemical Co., Ltd. Epigallocatechingallate (EGCG, 98 %) were purchased from XuanChengBaiCao Plant Industry and Trade Co., Ltd. All of the chemicals were used without further purification. Deionized water (DIW, 18.2 MΩ) was used for all solution preparations.

Synthesis of Au-PANFs precursor solution

The first step involved the synthesis of AuNPs in PAN/DMF solution via an *in situ* reduction method.[41] Briefly, 6 g PAN powder was dissolved in 44 mL DMF under magnetic stirring at 65 °C to get a homogenous solution. Then, 0.30 mmol $HAuCl_4 \cdot 4H_2O$ was added into the PAN/DMF solution and the mixture were stirred at 65 °C for 1 h. At last, 0.025 g EGCG was immediately added to the above mixture and the mixture was stirred by magnetic agitator for 3 h. Therefore, the mass fraction of PAN in the DMF solution was 12 wt% and the mass ratio of HAuCl4·4H2O and the PAN powder was 1.0 wt%.

Fabrication of the PANFs and Au-PANFs nanofibrous mats

The PAN/DMF (12 %) and Au-PANFs precursor solution with mass ratio of 1.0 wt% ($HAuCl_4 \cdot 4H_2O$ to PAN) was used to prepare nonwoven mats via electrospinning technique. The precursor solution was transferred into a syringe with a stainless copper needle at the tip. The needle was connected to a high voltage power supply. The applied voltage was 12 kV, the needle to collector distance was 12 cm and the flow rate of the solution was 0.6 mL/h. All experiments were performed at room temperature. The electrospun PANFs and Au-PANFs nanofibrous mats were collected onto a piece of aluminum foil.

Fabrication of CNFs and Au-CNFs nanofibrous mats

The as-collected electrospun PANF and Au-PANFs nanofibrous mats were peeled off from the aluminum foil and placed into a home-built CVD tube furnace for heat treatment. The nanofibrous mats was heated to 280 °C in air at a rate of 5 °C/min and maintained for 6 h for stabilization, then the samples were heated up to 800 °C at a rate of 5 °C/min under Ar gas flow (50 Sccm) for the graphitization. The desired graphitization temperature was held constant for 8 h and then the products were cooled to room temperature under Ar atmosphere.

Fabrication of the Au-CNFs nanofibers biosensors for H_2O_2 Detection

For the fabricating procedure of the Au-CNFs/GCE biosensor, the glassy carbon electrode (GCE) with a diameter of 3 mm was polished carefully using alumina slurry as a polisher to get a mirror-like surface, followed by rinsing with DIW and ethanol and then drying by nitrogen. The Au-CNFs fibrous mat was glued by Nafion aqueous solution (1 wt%) on the pretreated GCE and left to dry by N_2 at room temperature. The modified electrode was washed gently with DIW and then soaked in PB at 4 °C. This modified electrode is denoted as Au-CNFs/GCE. The control sample, CNFs was fabricated using similar procedures for the preparation of CNFs/GCE biosensors. All the modified electrodes were stored at 4 °C in a refrigerator before further characterizations.

Electrocatalytic measurement

Amperometric experiments were conducted with a CHI660H workstation (Shanghai Chenhua, Shanghai). All experiments were carried out using a conventional three-electrode system in 0.1 M PBS, where CNFs/GCE and Au-CNFs/GCE were used as the working electrode, a platinum foil as the auxiliary electrode and a saturated Ag/AgCl electrode as the reference electrode. The buffer was purged with high-purity nitrogen for at least 30 min prior to each amperometric experiment, and the nitrogen environment was then kept over the solution to protect the solution from oxygen. Electrochemical performances of the fabricated electrodes were tested using a three-electrode system by cyclic voltammetry (CV).

Instrumentation

The morphology evolutions of the PANFs, CNFs, Au-PANFs, Au-CNFs, Pt-PANFs and Pt-CNFs were characterized by a JSM-2100 transmission electron microscopy (JEOL, Japan) at an acceleration voltage of 200 kV and a JSM-6700F FE-SEM (JEOL, Japan) at an acceleration voltage of 3 kV. X-ray photoelectron spectra of the products were recorded using an X-ray photoelectron spectrometer (Kratos Axis Ultra DLD) with an aluminum (mono) K_α source (1486.6 eV). The aluminum K_α source was operated at 15 kV and 10 mA. Fourier transform infrared (FTIR) spectra were recorded on a Nicolet 5700 FTIR spectrometer in transmittance mode at a resolution of 4 cm^{-1} and 32 scans in the range from 4000 nm to 400 nm. XRD patterns of the nanofibrous mats were characterized with a SIEMENS Diffraktometer D5000 X-ray diffractometer using Cu K_α radiation source at 35 kV, with a scan rate of 0.02^o 2θ s^{-1} in the 2θ range of 10-80°. Raman spectra of all the samples were recorded by a RenishawinVia Raman microscope using a 532 nm laser excitation source. The excitation light intensity in front of the objective was 10 mW with a spectral collection time of 1s. The integration time for our measurements was set to 10 s. The high-angle annular dark field scanning TEM (HAADF-STEM) image, STEM mapping and line-scan energy dispersive X-ray spectroscopy (EDX) were recorded by a STEM (Tecnai G2 F30 S-Twin, Philips-FEI) at an acceleration voltage of 300 kV.

Results and discussion

The morphologies of the electrospun polyacrylonitrile nanofibers with embedded AuNPs (Au-PANFs) and carbon nanofibers with immobilized AuNPs on surfaces (Au-CNFs) were determined by using the FE-SEM and TEM characterizations. As shown in Figure 1a, the distinct and continuous Au-PANFs are straight and have smooth surfaces with an average diameter of about 512 ± 54 nm. The hybrid nanofibers are up to hundreds of micrometers in length, leading to high surface-to-volume ratios. In addition, no AuNPs can be seen on the surfaces of the Au-PANFs. However, from the TEM image of Au-PANFs shown in Figure 1b, small AuNPs with an average diameter of 2.3 ± 0.5 nm are evenly dispersed in the whole PANFs, indicating that the AuNPs are mainly embedded in internal PANFs. In addition, the inset in Figure 1b exhibits a HRTEM image of AuNPs, showing lattice fringes of the Au (111) plane with an interplaner distance of 0.23

nm.

Compared with the smooth surfaces of Au-PANFs, as shown in Figure 1d, large amounts of AuNPs were immobilized on the surfaces of CNFs. It means that after the graphitization process, the initial AuNPs embedded in internal PANFs broken through the nanofiber and formed on external surfaces of CNFs. The average diameter of the Au-CNFs decreases to 200 ± 44 nm after graphitization, indicating the significant shrinkage of the nanofibers. TEM image of Au-CNFs exhibits small and uniform AuNPs distributed on CNFs and the lattice fringes shown in inset in Figure 1e are visible with a spacing of about 0.23 nm, which corresponds to the lattice spacing of the (111) planes of Au.[41] Meanwhile, after the graphitization treatment at 800 °C, the diameter of AuNPs formed on the surfaces of CNFs increased to 5.6 ± 0.7 nm and no aggregated NPs are observed.

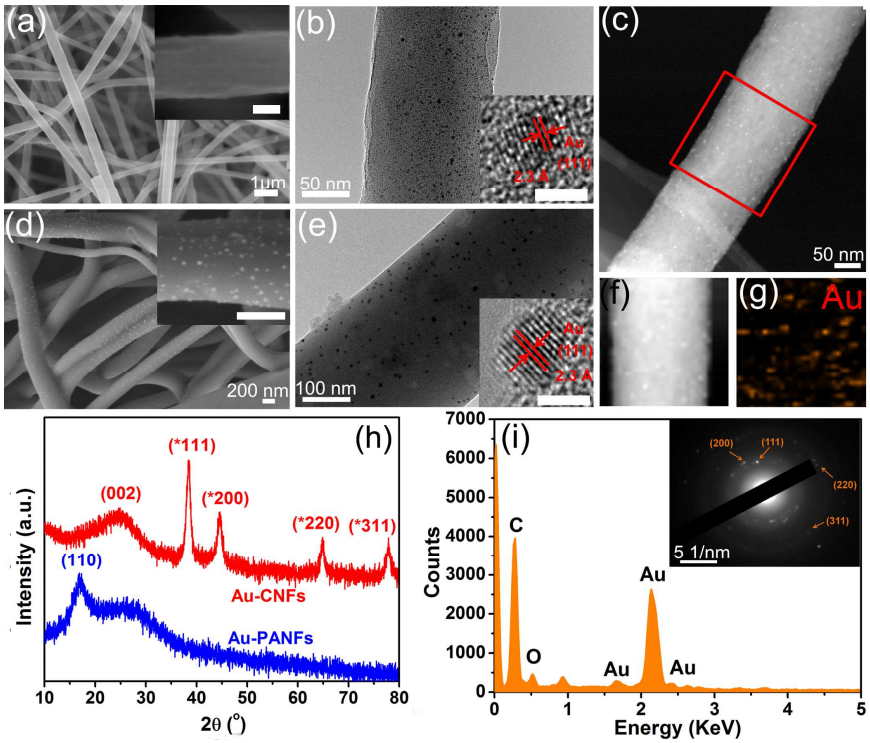

Figure 1 FE-SEM and TEM images of the (a, b) Au-PANFs and (d, e) Au-CNFs graphitized at 800 °C. Insets in Figure 1a and d are the high-magnification FE-SEM images of the Au-PANFs and Au-CNFs (scale bar 200 nm). Insets in Figure 1b and 1e are the HRTEM images of the AuNPs embedded in PANFs and on the surfaces of CNFs, respectively (scale bar 2 nm). (c, f) HAADF-STEM images of the Au-CNFs and the (g) STEM-EDS mapping image of the selective area of Au-CNFs. (h) XRD patterns of the Au-PANFs and Au-CNFs nanofibrous mats. (i) EDX spectrum of the Au-CNFs. Inset in Figure 1i is the SAED pattern of the Au-CNFs.

The interfacial structures of Au-CNFs can be resolved in greater detail by HAADF-STEM imaging (Figure 1c). HAADF-STEM image of the Au-CNFs can also indicate that the AuNPs are evenly immobilized on the surfaces of CNFs. As shown in Figure 1c and 1f, it is apparent that the brighter spots are the AuNPs, and the STEM-EDS mapping (Figure 1g) demonstrates that the quasi-spherical shapes of the AuNPs are immobilized on the external surfaces. Compared with Figure 1f, the positions of AuNPs in mapping image (Figure 1g) are nearly consistent with the AuNPs anchored on CNFs.

XRD patterns can provide much information about the crystal structures of Au-PANFs and Au-CNFs. As shown in Figure 1h, the Au-PANFs nanofibrous mats exhibit a sharp peak and a broad band, locating at 16.9° and 27.7°, which are ascribed to the PAN crystalline phase of (110) plane and amorphous phase.[43-44] However, there are no diffraction peaks of Au crystals emerged on the XRD pattern. Meanwhile, the representative diffraction peak (002) of the stacked graphite layers (JCPDS 75-1621) in the Au-CNFs is detected at 2θ= 24.7°, demonstrating the crystalline structures of graphitic carbon in the nanofibers.[45-46] Interplanar d-spacing of the graphite layers were calculated using the Bragg's Law.[45-46] By using λ = 0.154 nm (Cu K_α), the calculated value of d_{002} of Au-CNFs is 3.60 Å. Compared with Au-PANFs, four new strong peaks appeared at 38.3°, 44.4°, 64.8°, and 77.8°, which are consistent with the (111), (200), (220) and (311) planes of Au crystal, respectively (JCPDS 04-0784).[47-48] The strong differences in the diffraction peaks of the Au crystal between the Au-PANFs and Au-CNFs demonstrate that the Au-CNFs have much exposed AuNPs on the surfaces, which are consistent with the FE-SEM and STEM results. We have further preformed the EDX spectroscopy of Au-CNFs, and Figure 1i shows the Au, C and O elements, confirming the presence of AuNPs. The SAED pattern (inset in Figure 1i) recorded on the mapping region of Au-CNFs as indicated by the red square in Figure 1c further verifies that the AuNPs are polycrystalline in nature and consist of face-centered cubic-phase nanocrystallines. The concentric diffraction rings from inside to outside are indexed to the (111), (200), (220), and (311) planes of Au crystal.[18,48]

XPS was used to investigate the chemical states of the surfaces of Au-PANFs and Au-CNFs. As shown in Figure 2a, the Au 4f XPS spectra of Au-PANFs can be deconvoluted to two

peaks at 88.0 and 84.3 eV, which are associated with the binding energies (BE) of Au $4f_{7/2}$ and Au $4f_{5/2}$, respectively. Compared with the BE of Au^0 (87.7 eV and 84.0 eV), the relative higher BE of Au 4f indicates that the AuNPs embedded in PANFs are surrounded by the PAN molecules, leading to a substantial electron donation from AuNPs to the stabilizer molecules.[41,49-50] Tanaka and Negishi *et al.* have reported that the relatively high binding energy of Au 4f was due to the binding of surface Au atoms in AuNPs with the stabilizer or passive molecules surrounding the nanoparticles, which led to a substantial electron donation from AuNPs to the stabilizer molecules.[49-50] These indicate that the AuNPs were embedded in the inner PANFs and surrounded by large amounts of PAN molecules.

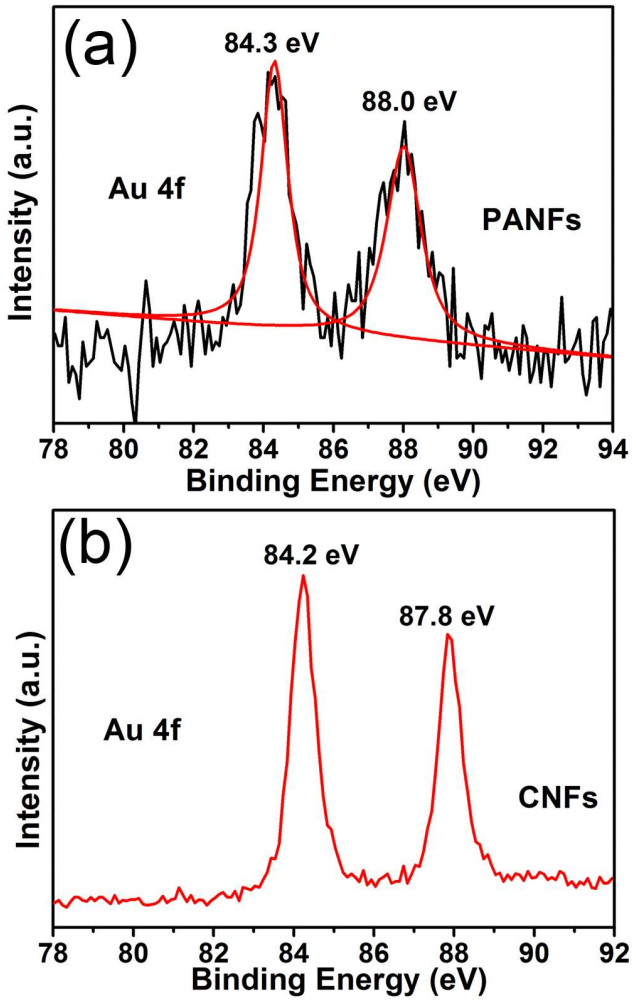

Figure 2 XPS spectra of the Au 4f of (a) Au-PANFs and (b) Au-CNFs graphitized at 800 °C.

Focusing on the XPS spectrum of Au-CNFs, two sharp and distinct peaks can be observed at 84.2 and 87.8 eV. Compared with that of the Au-PANFs, the BE of Au 4f of Au-CNFs are close to the BE of Au0, indicating that the AuNPs on the surfaces of CNFs surrounded with few molecules. A few molecules around the exposed AuNPs on CNFs lead to weaker substantial electron donation, and the small changes in the BE of Au 4f. The intensity of the Au 4f peaks of Au-CNFs is much higher than that of Au-PANFs, demonstrating that the Au-CNFs have more exposed AuNPs on the surfaces of the nanofibers. The XPS results are consistent with the FE-SEM, STEM and XRD results and more discussion can be found in the following studies.

To investigate the evolutions of the AuNPs transferred from the interior to the external surfaces, we performed a control experiment to study the graphitization of the PANFs. The morphologies, microstructures and crystal structures were examined by TEM, FESEM, STEM, XRD and Raman characterizations. Figure 3a shows the amorphous structure of PANFs and as shown in Figure 3b, the carbonaceous matrix of CNFs was constructed by graphitic carbon layers. The insets in Figure 3b show the lattice spacing of 0.36 nm corresponding to the (002) lattice plane of graphite and the typical diffraction pattern of the CNFs, reflecting randomly oriented polycrystallites.[45-46] Therefore, along with the carbonization from PANFs to CNFs, the amorphous structures of PANFs converted to the graphitic carbon layered structures.

The HAADF-STEM and STEM-EDS mapping images of CNFs clearly show three different elements, which are ascribed to carbon, oxygen and nitrogen. We have further performed line-scanned EDX spectra on individual CNF. Figure 3l shows the line-scanned EDX spectra of CNFs along the red-line (Figure 3f) across the nanofiber, which clearly shows the existences of carbon, oxygen and nitrogen.

Comparing the FE-SEM images of PANFs with CNFs, the average diameters of nanofibers decreased from 560 nm to 200 nm, indicating the significant shrinkage of the PANFs. Based on the above results, we suppose that the AuNPs transferred from the inner of PANFs to the outer of CNFs was caused by the carbonization process, and more experiments and discussion will be performed in the following studies. XRD patterns also indicate the structure conversion from PANFs to CNFs. As shown in Figure 3j, the PANFs mats exhibit two peaks, locating at 17.1° and 26.7°, which are ascribed to the PAN crystalline phase and amorphous phase, respectively. The broader diffraction peaks of CNFs centered at 24.1° and 44.1° are attributed to carbon (002) and (100) planes. The d_{002} calculated value of pure CNFs is 3.69 Å. Compared with the d_{002} value of graphite (0.335 nm), the expanded d_{002} value of CNFs (0.369 nm) and Au-CNFs (0.360 nm) implies that the graphene layers are displaced due to many layer-sequential mismatches occurring in the CNFs and that there is much space for energy storage.[24,45-46]

The Raman spectrum of the PANFs doesn't show any peaks in the range from 1000 to 2000 cm^{-1}, while the CNFs exhibits two fundamental vibrations, which are observed at 1357 and 1577 cm^{-1}.The primary peak (D band) corresponds to the breaking symmetry caused by defects or structural disorders, while the later peak (G band) is related the in-plane tangential stretch vibration mode of graphitic layer.[48,51] The intensity ratio of D and G bands (I_D/I_G) was calculated to be 1.09, showing that the CNFs indeed composed of graphitic rolls mixed with a small amount of amorphous carbon and a number of pores.

FTIR and XPS were used to study the evolutions in chemical structures, surface compositions and chemical states of the PANFs and CNFs during the graphitization process. As shown in Figure 4a, the FTIR spectra of PANFs, pre-oxidation PANFs at 280 °C (PANOF) and CNFs graphitized at 1000 °C were performed to investigate the evolutions in chemical structures

during the graphitization process.

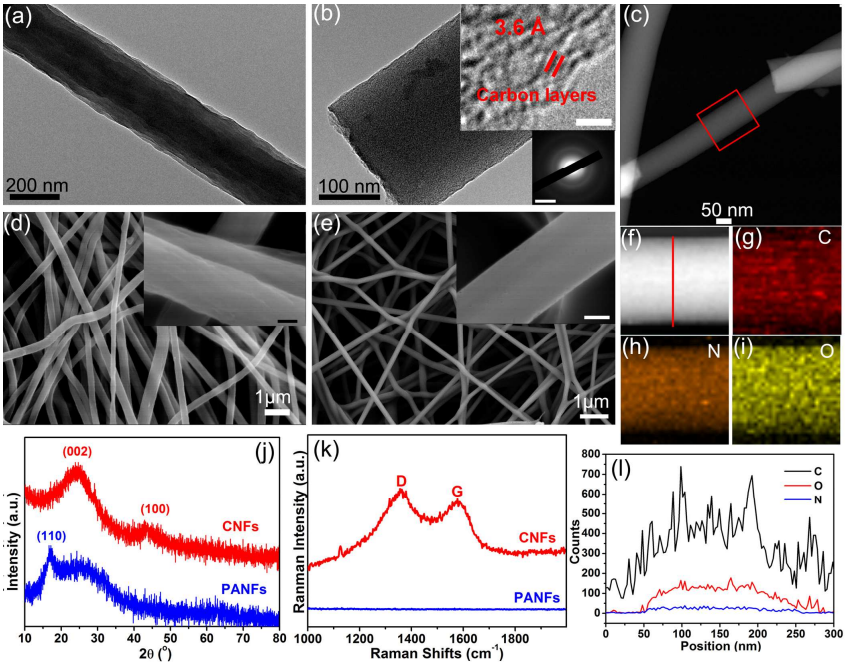

Figure 3 TEM and FE-SEM images of the (a, d) PANFs and (b, e) CNFs graphitized at 1000 °C. (c, f) HAADF-STEM images of the Au-CNFs and the (g-i) STEM-EDS mapping images of the selective area of CNFs. (j) XRD patterns and (k) Raman spectra of the PANFs and CNFs nanofibrous mats. (l) Line-scan EDX spectra of the CNF. Insets in Figure 3b are the HRTEM image and SAED pattern of the CNFs (scale bars, 2 nm and 5 1/nm). Inset in Figure 3d and 3e are the high-magnification FE-SEM images of CNFs (scale bars, 200 nm and 100 nm).

The PANFs displays a broad band centered at 3472 cm^{-1} ascribed to the stretching vibration of O-H groups. The other three characteristic peaks at 1670, 2242 and 2931 cm^{-1} correspond to the C=O stretching in carboxylate groups, C≡N stretching in nitrile groups and C-H stretching in C-H and CH2 groups, which are consistent with the previous literatures.[41,43,52] After the pre-oxidation at 280 °C, the FTIR spectrum of PANOFs exhibits relative weaker intensity of C≡N peaks (2242 cm^{-1}). In addition, the two strong peaks located at 1590 and 1372 cm^{-1} are ascribed to the C=N and C=C stretching vibration and the C-H In-plane blending vibration, indicating the conversion from the C≡N structure to C=C-C=N structure during the pre-oxidation process.[52-53] What's more, a strong peak ascribed to the C=C-H bending vibration can be observed at 805 cm^{-1}. The above FTIR results demonstrate that the C≡N structures were converted to C=C-C=N structure, forming the aromatic structures. After the carbonization at 800 °C, the characteristic peaks for O-H, C≡N are vanished, the peaks located at 1574 and 1205 cm^{-1} are attributed to the C=C or C=N stretching vibration and C-N bending vibration. Such chemical changes can clearly demonstrate the chemical structure conversion during the graphitization process.

The XPS spectra of PANFs and CNFs nanofibrous mats are shown in Figure 4b-f. As shown in the C 1s spectra of PANFs in Figure 4b, three different types of carbon with different chemical states are observed at 284.7, 285.7 and 288.3 eV, respectively. These peaks are ascribed to the carbon atoms in different functional groups: the C-C, the C in C≡N bonds and the C in C=O bonds, respectively.[53-54] Meanwhile, the CNFs show a distinct peak located at 284.8 eV corresponding to the graphitized carbon. The other two weaker peaks located at 286.3 and 289.3 eV are ascribed to the C-O or C-N bonds and C=O bonds. The C=O groups of PANFs are due to the two different chemical environments of oxygen in methyl acrylate (PAN contains 10 wt% of methyl acrylate), while the C=O groups of CNFs are due to the oxygen-containing groups on the surface of the nanofibers, which are similar to those of our previous studies.[41] The O 1s XPS spectra of PANFs exhibit two peaks at 532.5 eV and 534.2 eV associated with the chemical environments of oxygen in carbonyl groups of methyl acrylate. Focusing on the CNFs, the O 1s show two peaks located at 530.2 and 532.1 eV may be due to adsorbed oxygen, carbonyl groups.

The relative higher binding energy peak at 533.8 eV possibly originates from absorbed H_2O, which is similar with the previous reports.[53-55] The N 1s spectra of the PANFs exhibit a significant peak at 398.8 eV and it can be assigned to the nitrogen atoms that bond with carbon atoms in the form of C ≡ N bonds.[51] Meanwhile, after the graphitization process, the CNFs show two very weak bands centered at 399.0 eV and 401.7 eV, which are attributed to the C ≡ N species and pyridinic nitrogen, demonstrating the formation of C=C-C=N structure. The above results confirm the conversion in the chemical structures from C≡N to C=C-C=N structure during the graphitization process. Based on the FTIR and XPS results, the conversion in chemical structures from PANFs to CNFs is illustrated in Figure S1. The graphitization processes for the conversion from PANF to CNFs are divided into three steps: oxidative stabilization, high-temperature carbonization, and graphitization.[56] The

stabilization of PANFs treated at 280 °C can ensure both the molecules and the molecular orientation. At this stage, the adjacent cyano groups reacted with each other and thus, the macromolecules cross-link together through the chemical bonds. Through the carbonization and graphitization process, the chemical structures covert from C≡N to C=C-C=N structure, forming the aromatic structure and then graphene layered structures.

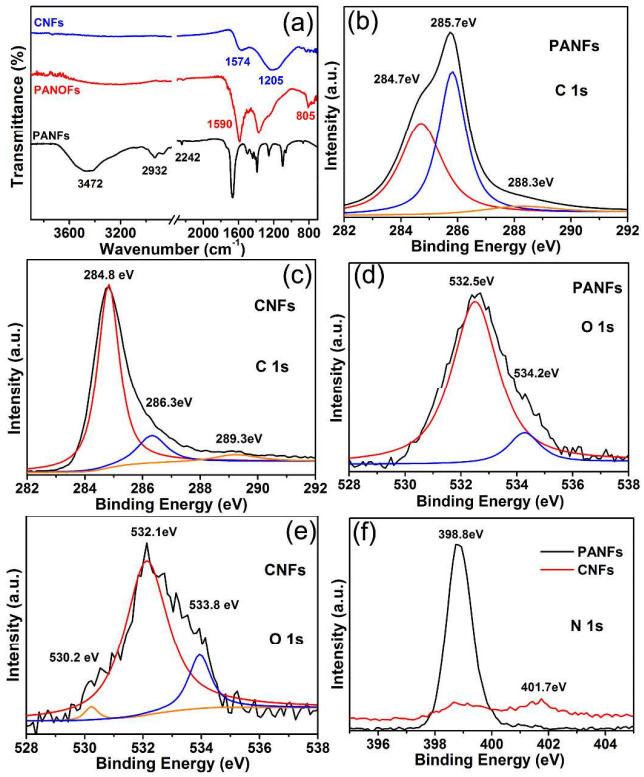

Figure 4 (a) FTIR spectra of the PANFs, pre-oxidation PANFs at 280 °C and CNFs carbonized at 1000 °C. XPS spectra of C1s of (b) PANFs and (c) CNFs. XPS spectra of O 1s of (d) PANFs and (e) CNFs. (f) XPS spectra of N 1s of PANFs and CNFs.

Based on the above results, the graphitization process would lead to the significant shrinkages of the nanofibers and the structure conversions from amorphous to graphene layered structures. The high graphitization temperature and fast heating rate could lead to the dramatic shrinkage of the nanofibers, which are the key for the emigration of AuNPs from the inner to the outer of the nanofibers.

In the follow study, we performed the control experiments for the conversion from Au-PANFs to Au-CNFs with different graphitization temperatures and heating rates. As shown in Figure 5a and 5e, the Au-PANFs with higher mass ratio of $HAuCl_4 \cdot 4H_2O$ (2.5 wt %) were synthesized to explore the emigrations and evolutions of the AuNPs. As shown in Figure 5a, large amounts of spherical AuNPs with average diameter of about 2.5 ± 0.6 nm are evenly embedded in the interior of PANFs. From the edges of the PANFs (inset in Figure 5a) and the FE-SEM image of the Au-PANFs, there are nearly no AuNPs can be observed at the surfaces of PANFs. After the graphitization at 600 °C, the average diameter of spherical AuNPs increases to 4.1 ± 1.1 nm and the AuNPs trend to emigrate to the edges of the CNFs, which can be observed in Figure 5b and 5f. From Figure 5f, the FE-SEM image of Au-CNFs (600 °C, 2 °C/min) exhibits that a lot of AuNPs break through the CNFs and immobilize on the surfaces of CNFs. In addition, there are still space among the AuNPs and no aggregated AuNPs.

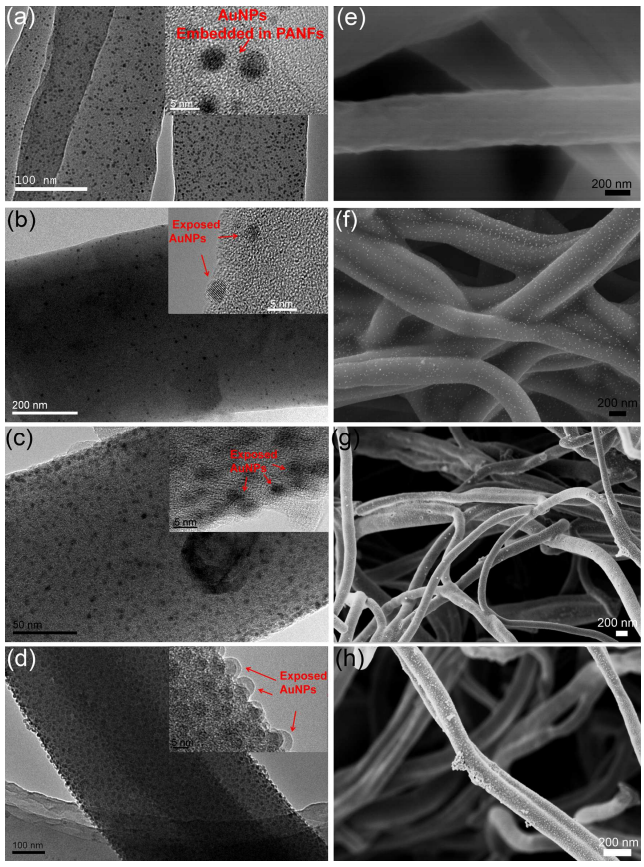

Figure 5 (a) TEM and (e) FE-SEM images of the Au-PANFs with the mass ration of 2.5 wt % (PAN and $HAuCl_4$). TEM and FE-TEM images of Au-CNFs with various graphitization temperatures at (b, f) 600 °C, (c, g) 800 °C and (a, h) 1000 °C, respectively. Insets are the corresponding HRTEM images of the Au-PANFs and Au-CNFs. The heating rate of the graphitization process is 2 °C/min.

Meanwhile, the diameter of Au-PANFs is about 530 ± 52 nm while the Au-CNFs is about 320 ± 64 nm, indicating the significant shrinkage of the nanofibers. With increased graphitization temperature at 800 °C, as shown in 5c and 5g, more and more spherical AuNPs can be found on the surfaces of CNFs and the distance among each AuNPs becomes closer. In addition, it can be seen from the HRTEM image (inset in Figure 5c) of the edges of Au-CNFs that the AuNPs are emigrating from the interior of CNFs. The average diameter of the AuNPs increases to 4.9 ± 1.2 nm and the diameter of the Au-CNFs decreases to 260 ± 43 nm, indicating the continuous emigration of AuNPs and shrinkage of the nanofibers. When the temperature increased to 1000 °C, most of the spherical AuNPs are exposed on the surfaces of the CNFs and the AuNPs are right next to each other (Figure 5d). The average diameter of the AuNPs increased to 6.9 ± 1.4 nm and the diameter of the Au-CNFs decreased to 210 ± 45 nm. However, along with the large amounts of exposed AuNPs and significant shrinkage, there are still no serious

aggregated NPs, demonstrating that at the low heating rate, the Au-CNFs with higher density of exposed AuNPs with small and uniform sizes can be obtained.

Table 1 XPS atomic concentrations, mass concentrations and Au 4f BE of the Au-PANFs and CNFs graphitized at 600, 800, 1000 °C/min at a heating rate of 2 °C/min.

Samles	Au 4f binding energy (eV)	Atomic concentrations (%)	Mass concentrations (%)
Au-PANFs	84.3, 88.0	0.06	0.92
Au-CNFs-600	84.2, 87.9	0.21	3.12
Au-CNFs-800	84.2, 87.8	0.38	4.92
Au-CNFs-1000	84.1, 87.8	0.95	8.04

Table 1 summarized the XPS atomic concentrations, mass concentrations and Au 4f BE of the Au-PANFs and CNFs graphitized at 600, 800, 1000 °C/min at a heating rate of 2 °C/min. In our present investigations, we used the same Au-PANFs samples to prepare Au-CNFs nanofibrous mats and it means that the mass concentration of Au in PANFs before graphitization is constant. The Au-PANFs exhibits the lowest atomic and mass concentrations of Au, which are 0.06 and 0.96 %, suggesting the lowest density of exposed AuNPs on the surfaces. Through graphitization at 600, 800, and 1000 °C, the atomic and mass concentrations increase to 0.21 % and 3.12 %, 0.38 % and 4.92 %, and 0.95 % and 8.04 %, demonstrating the increased densities of exposed AuNPs on the surfaces of CNFs. Compared with the BE of Au 4f of Au-PANFs (84.3 and 88.0 eV), the Au-CNFs graphitized at 600, 800, and 1000 °C exhibit relative lower BE. With increased graphitization temperatures, the BE of Au 4f get closer to the BE of Au^0 (87.7 eV and 84. 0 eV), suggesting the emigration of AuNPs through the matrix of nanofibers. The changes in the mass concentration and atomic concentration of Au-PANFs and Au-CNFs-600, Au-CNFs-800 and Au-CNFs-1000 can strong indicate the emigration of AuNPs from the inner to the external CNFs.

Figure 6 shows the TEM and FE-TEM images of Au-CNFs with various graphitization temperatures at 600, 800 and 1000 °C, respectively. The heating rate of the graphitization process is 5 °C/min. As shown from Figure 6a to Figure 6c, a series of evolutions can be clearly observed. With increased graphitization temperatures from 600 to 1000 °C, compared with the AuNPs embedded in PANFs (3.4 ± 0.6 nm), the average diameters of the AuNPs increased to 5.8 ± 1.1, 8.3 ± 2.3 and 10.2 ± 2.7 nm, respectively, which are similar with the Figure 6. In addition, compared with those of Au-PANFs (530 ± 52 nm), the diameters of Au-CNFs decreases to 306 ± 67, 234 ± 52, and 195 ± 48 nm, respectively, indicating the enormous shrinkage of nanofibers. The evolutions of the emigrations of AuNPs can be clearly observed in the HRTEM images in Figure 6a, 6b and 6c. At 600 °C, a little area of AuNPs are exposed and coated by three graphene layers, indicating the emigrations of AuNPs. Both the fringe of the AuNP and graphitic carbon shells can be simultaneously observed in the insets Figure 6a. The lattice spacings of 0.23 nm and 0.36 nm are ascribed to the (111) plane of Au crystal and the (002) lattice plane of graphite, respectively.

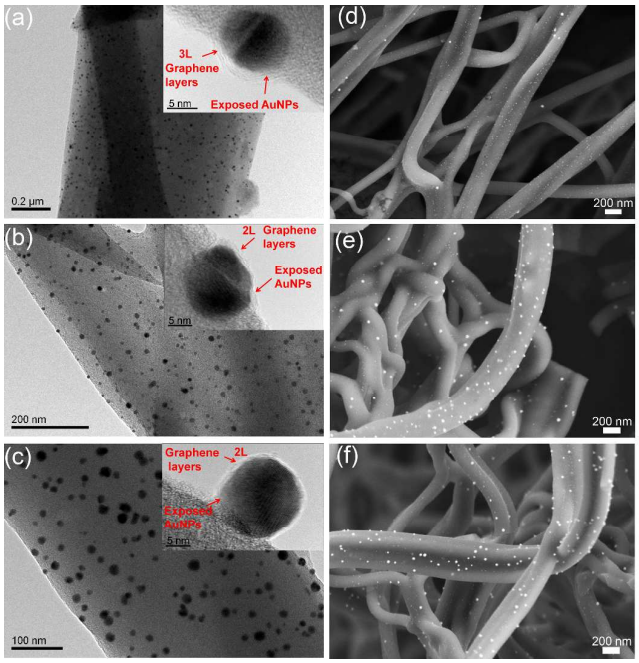

Figure 6 TEM and FE-TEM images of Au-CNFs with various graphitization temperatures at (a, d) 600 °C, (b, e) 800 °C and (c, f) 1000 °C, respectively. Insets are the cor-responding HRTEM images of the AuNPs. The heating rate of the graphitization process is 5 °C/min.

Typically, with increased to 800 °C, more area of AuNPs are exposed from the inner of the nanofibers and coated by two graphene layers. With continuous increased to 1000 °C, the AuNPs are almost broken through the nanofibers and immobilized on the surfaces (Figure 6c). The exposed AuNPs are also coated by two graphene layers. The complete emigration process of AuNPs from the interior of PANFs to the exterior of CNFs can be clearly observed. The exposed AuNPs are surrounded by several graphene layers while the AuNPs embedded in PANFs are surrounded by large amounts of PAN macromolecules, which are consistent with the XPS results (Figure 2). Note that as shown in Figure 6c and 6f, the phenomena of adjacent AuNPs became serious, indicating the aggregation of AuNPs.

When the heating rate increased to 10 °C/min, as shown in Figure 7a and 7d, the Au-CNFs (600 °C) exhibit high density of exposed AuNPs on the surfaces of CNFs. Compared with Au-PANFs, the average diameter of the AuNPs increases to 10.7 ± 2.8 nm and at this temperature and heating rate, the AuNPs still remain spherical shapes. With the temperature increased to 800 °C, the exposed AuNPs tend to collide with adjacent NPs and grew up to larger sized AuNPs with irregular shapes (Figure 7b and 7e). Figure 7c and 7f shows the Au-CNFs carbonized at 1000 °C, and the spherical AuNPs embedded in PANFs grew up to larger sized AuNPs with irregular shapes immobilized on the

CNFs, indicating the emigrations and ripening phenomena of AuNPs. The average diameter of the AuNPs with irregular shapes graphitized at 800 and 1000 °C are 18.2 ± 3.7 and 25.5 ± 5.1 nm. Compared with Au-PANFs, the diameter of Au-CNFs decreased to 260 nm ± 42, 205 ± 38 and 180 ± 36 nm, demonstrating the remarkable shrinkage of the nanofibers.

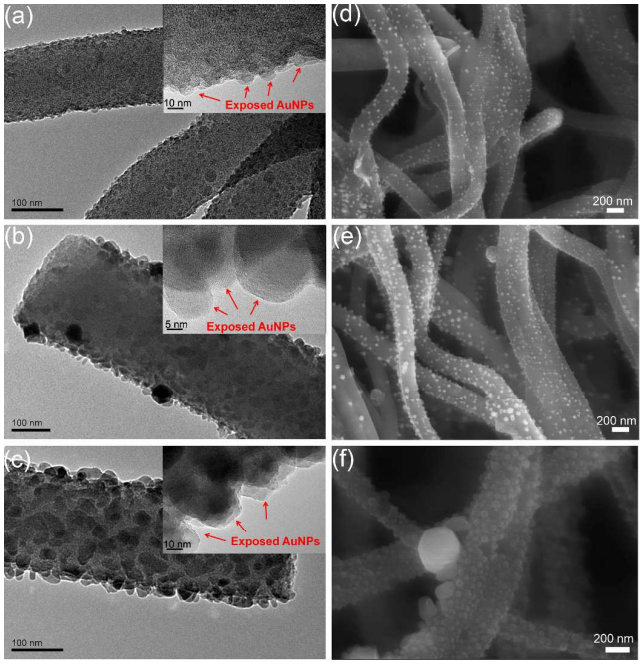

Figure 7 TEM and FE-TEM images of Au-CNFs with various graphitization temperatures at (a, d) 600 °C, (b, e) 800 °C and (c, f) 1000 °C, respectively. Insets are the cor-responding HRTEM images of the AuNPs. The heating rate of the graphitization process is 10 °C/min.

The heating temperature ranged from 300 to 500 °C belongs to the carbonization process. At low heating rate (2 °C/min) and heating temperature (600 °C), the AuNPs with low exposed area have already emerged from the nanofibers (Figure 6b). However, the AuNPs did not completely come out from the internal nanofibers until the temperature heated to the 1000 °C (Figure 6d). However, at 1000 °C, the exposed AuNPs still remain small sizes (6.9 ± 1.4 nm) and uniform spherical shapes without any aggregated NPs. With increased heating rate to 5 °C/min, the emigration of AuNPs became faster in comparison with Figure 7. The diameters of the AuNPs of Au-CNFs increase from 5.8 ± 1.1 to 10.2 ± 2.7 nm along with the increased heating temperatures from 600 to 800 °C, indicating that the faster heating rate results in the greater shrinkage and collisions of AuNPs to form larger sized AuNPs. Based on the above results, with the heating rate at 5 °C/min and graphitization temperature at 1000 °C, the AuNPs can completely expose on the surfaces of CNFs. Table 2 summarized the statistics of the diameter of AuNPs embedded in PANFs and AuNPs immobilized on CNFs at different graphitization temperatures of 600, 800 and 1000 °C and heating rates of 2, 5, 10 °C/min.

It can be concluded that the higher graphitization temperature and faster heating rate can strong influence the shrinkage of the nanofibers and the sizes of AuNPs. In addition, the higher graphitization temperature and fast heating rate could result in the aggregation of AuNPs into larger ones that are inclined to be exposed on the surface of the CNFs. Therefore, these results can strong support the assumption, that is, during the graphitization, with the conversion from amorphous structures to graphene layered structures, the pre-formed AuNPs embedded in PANFs can move around the random oriented graphene layers. Meanwhile, along with the shrinkage of nanofibers, the AuNPs can emigrate to the surfaces of the CNFs.

Table 2 The statistics of the AuNPs embedded in PANFs and AuNPs immobilized on CNFs at different graphitization temperatures and heating rates.

Samples	Average diameters of AuNPs (nm)	Average diameters of nanofibers (nm)	Heating rates (°C/min)
Au-PANFs	2.5 ± 0.6	530 ± 52	
AuCNFs-600	4.1 ± 1.1	320 ± 64	2
AuCNFs-800	4.9 ± 1.2	260 ± 43	2
AuCNFs-1000	6.9 ± 1.4	210 ± 45	2
AuCNFs-600	5.8 ± 1.1	306 ± 67	5
AuCNFs-800	8.3 ± 2.3	234 ± 52	5
AuCNFs-1000	10. 2 ± 2.7	195 ± 48	5
AuCNFs-600	10. 7 ± 2.8	260 ± 42	10
AuCNFs-800	18.2 ± 3.7	205 ± 38	10
AuCNFs-1000	23.5 ± 5.1	180 ± 36	10

To further investigate the emigration of the AuNPs on the external surfaces of AuNPs, we performed a control experiment to count the numbers of AuNPs on CNFs. Figure 8 shows the TEM and HAADF-STEM images of the Au-CNFs with low mass ratio of $HAuCl_4$ (0.5 wt %) treated at 1000 °C (5 °C/min). As shown in Figure 8a, the AuNPs are evenly dispersed in the CNFs and however, it cannot be determined whether the AuNPs are embedded in the interior of CNFs or immobilized on the exterior of the CNFs. Focusing on the HAADF-STEM images of the Au-CNFs, it can be clearly observed that the AuNPs (bright spots) are indeed immobilized on the surfaces of the CNFs. The exposed density of the AuNPs in Figure 8b is almost consistent with the AuNPs dispersed in CNFs in Figure 8a. The STEM-EDS mapping images of the Au-CNFs taken randomly were further to investigate the locations of the AuNPs.

Figure 8c shows the mapping area of the Au-CNFs and Figure 8d exhibits the STEM-EDS mapping image of CNF constructed by carbon elements. Compared with the mapping area of CNFs in Figure 8c, the yellow bright spots in Figure 8e are constructed by Au elements and the shapes, locations and sizes are exactly the same. Twelve yellow spots (AuNPs) can be clearly observed, which are consistent with the numbers of the AuNPs in Figure 8c, confirming the exposed AuNPs on the surfaces of CNFs. As shown in Figure 8f, there are eleven AuNPs dispersed on CNFs. Compared with Figure 8f, the HAADF-STEM image of the same area also exhibits eleven AuNPs with the same locations, shapes and sizes, locating on the surface of the CNF. Therefore, at heating rate of 5 °C/min and graphitization temperature of 1000

°C, the initial AuNPs embedded in PANFs were emigrated to the surfaces of CNFs.

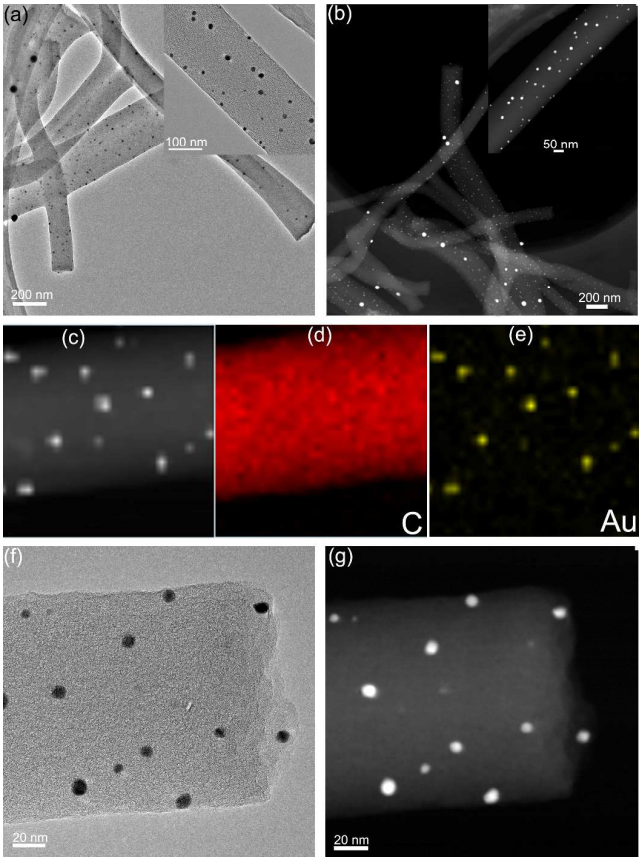

Figure 8 (a) TEM and (b) HAADF-STEM images of the Au-CNFs graphitized at 1000 °C (5 °C/min) with low mass ratio of $HAuCl_4$ (0.5 wt %). Insets are the corresponding high-resolution TEM and HAADF-STEM images of single Au-CNFs. (c) HAADF-STEM and (d, e) STEM-EDS mapping images of the randomly selective area of the Au-CNFs. (f) TEM and (g) HAADF-STEM images of the Au-CNFs taken at the same areas.

On the basis of the above investigations, a schematic is displayed in Figure 9 to summarize the behaviours of AuNPs emigrated from the interior of PANFs to the external surfaces of CNFs during the graphitization process. According to our previous study, the small and well-dispersed AuNPs embedded in PANFs were synthesized by an in situ reduction approach.[41-42] The PAN macromolecule with abundant cyano groups (C≡N) can effectively anchor the AuNPs because of the strong chelating effect.[41-42] In addition, the PAN macromolecules both acted as chelating agent and stabilizer to protect the AuNPs from aggregations, leading to uniform and well-dispersed AuNPs. During the carbonization process, the C≡N structure started to converted to C=C-C=N structure, forming the aromatic structures and the graphene layer structures. Without the stabilization of the C≡N groups, the pre-formed AuNPs embedded in PANFs can emigrated around the random oriented graphene layers.

It is reported that the metal NPs exhibit size-dependent meltings.[57] For particles of spherical geometry with diameter D:

$T_m/T_b=1-C/D$,

where T_m is the melting temperature of the NPs with diameter D, Tb is the melting temperature of bulk solids (Au: T_b = 1338K), C is the material constant (Au: C=1.1281 nm). As discussed above, the average diameter of the initial AuNPs embedded in PANFs is 2.5 ± 0.6 nm and according to the equation, the melting temperature of the AuNPs is 734 K (461 °C), which is below the graphitization temperatures at 600 °C. Therefore, when AuNPs were treated at elevated temperatures, the initial AuNPs melted into atom scale. The size of Au atoms is smaller than the spaces of graphene layers of the CNFs (0.37 nm) and therefore, the Au atoms can emigrate and diffuse through the graphene layers. In our case, the randomly oriented graphene layers provide many potential paths (nanochannels) connecting the inner nanofibers and the external environment. However, these paths are not straight, but tortuous, thus, the distance for atoms to pass the nanofibers to the surfaces is largely exceeding the nanofibers thickness.

At the same condition, the Au atoms closer to the surfaces of nanofibers had smaller migratory distances and preferentially emigrated to the surfaces. More and more preferentially migratory Au atoms were nucleated at the surfaces and grew up to NPs. The emigration rates and diffusion of Au atoms were strong depended on the graphitization temperatures and heating rates. Higher graphitization temperatures and heating rates lead to faster molecular movement, indicating the faster emigration and diffusion of Au atoms. Therefore, Au atoms with faster emigration and diffusion rates can easily exposed on the surfaces of nanofibers, while the slower ones still remain in the matrix of nanofibers. Along with the shrinkages of nanofibers, more and more Au atoms diffused and emigrated to the surfaces of the CNFs and grew up to AuNPs. The relative larger size of AuNPs immobilized on CNFs was caused by the aggregation of the small AuNPs because of the faster diffusion of Au atoms during the carbonization process. Because of the high treatment temperature and the emigration of the AuNPs, the neighboring AuNPs may collide with each other and then aged to larger AuNPs.

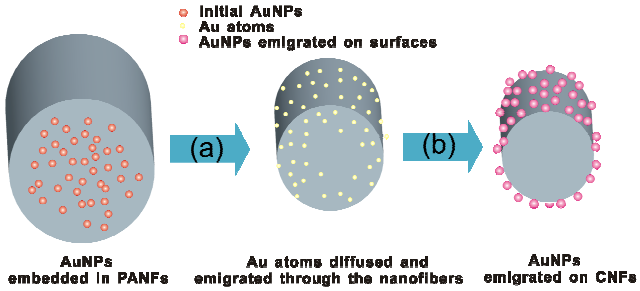

Figure 9 Schematics of the behaviours of AuNPs emigrated through the nanofibers during the graphitization process: (a) The melting of initial AuNPs embedded in PANFs and the diffusion and emigration of Au atoms through the matrix of nanofibers. (b) The Au atoms diffused and emigrated to the surfaces of the CNFs and grew up to AuNPs.

To confirm this new strategy is a general approach for the fabrication of CNFs-noble metal nanostructures, Pt-CNFs hybrid nanostructures were also prepared by the method. As shown in Figure 10a and 10c, the PtNPs with average diameter of 4.4 ± 0.9 nm were evenly dispersed in inner PANFs. After graphitization at 1000 °C with heat rate of 5 °C/min, most of the PtNPs were exposed on the surfaces of CNFs and diameter of PtNPs increases to 10.7± 2.5 nm. The observed phenomena are similar with the

Au-CNFs systems, indicating that the new strategy is not only applicable to the Au system but also employed for the fabrication of other noble metal-CNFs nanostructures.

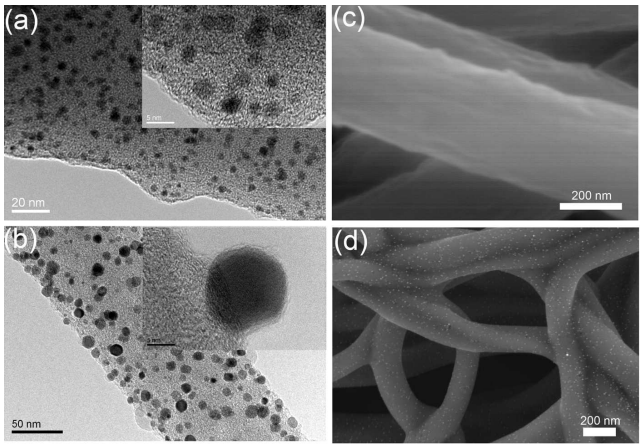

Figure 10 TEM and FE-SEM images of the (a, c) Pt-PANFs and (b, d) Pt-CNFs (1000 °C, 5 °C/min) hybrid nanostructures. Insets are the corresponding HRTEM images.

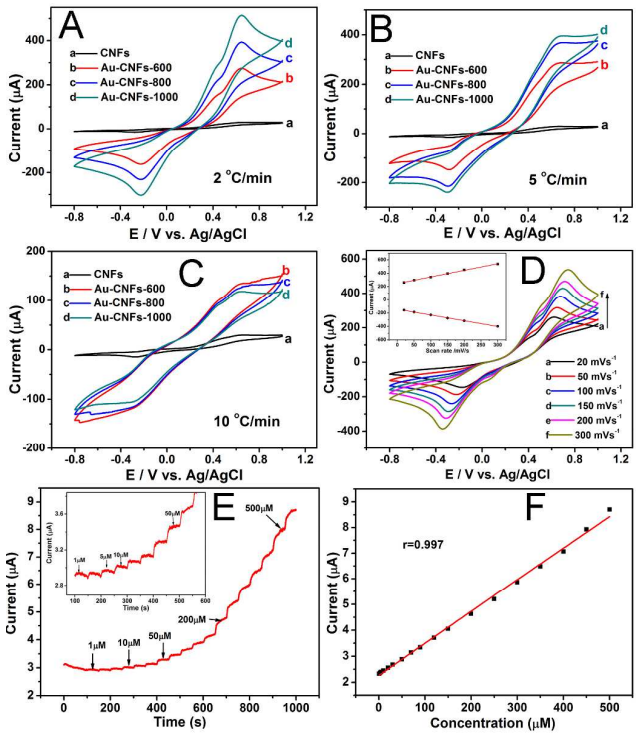

Figure 11 (A-C) The electrochemical properties of CNFs and Au-CNFs with different graphitization temperatures and heating rates. CVs of (a) CNFs/GCE, (b) Au-CNFs-600/GCE, (c) Au-CNFs-800/GCE and Au-CNFs-1000/GCE biosensor with 5.0 mM HQ in 0.1 M PBS in the presence of 5.0 mM H_2O_2 (scan rate, 50 mV s^{-1}). (D) CVs of Au-CNFs-1000/GCE (2 °C/min) in 1.0 mM H_2O_2 with different scan rates and the inset shows the relationship between the redox peak currents and scan rates; (E) Amperometric response of the fabricated Au-CNFs-1000/GCE (2 °C/min) sensor to successive addition of different concentration of H_2O_2 to 1.0 M PBS and inset shows the response of the sensor from 1 μM to 50 μM H_2O_2; (F) Relationship of the calibration curve and linear fitting curve between the currents and the H_2O_2 concentration.

Compared with the bulk metal electrode, such small, uniform and well-dispersed AuNPs immobilized on the surfaces of CNFs possess high ratio of surface atoms with free valences to the cluster of total atoms and can provide electrochemical reversibility for the redox reactions.[6-7] Figure 11 shows the cyclic voltammograms (CVs) of CNFs and Au-CNFs functionalized GCE with H_2O_2 in the presence of hydroquinone (HQ). According to the reported literatures[22,51], high graphitization temperatures would lead to the relative higher conductivity because of their increasing degree of graphitization of CNFs. Therefore, we performed the electrochemical properties of CNFs and Au-CNFs with different graphitization temperatures and heating rates to study their morphology-dependent electrochemical activities. As shown in Figure 11A, curve a is ascribed to the CVs of CNFs (graphitized at 1000 °C) with H_2O_2 in 5 mM HQ and much weak redox peaks can be observed. The curve b, c and d are ascribed to the CVs of Au-CNFs graphitized at 600, 800, and 1000 °C with a heating rate of 2 °C/min. Comparing to the CVs of CNFs (curve a) with Au-CNFs in HQ with H_2O_2 (curve b to curve d), significant redox peaks of Au-CNFs are obtained, indicating the electroactive property of Au-CNFs. It can be clearly observed even the sizes of the AuNPs on CNFs increased from 4.1 to 6.9 nm, the intensity of the redox peaks significantly promoted with the increased density of exposed AuNPs (Figure 11A, curve b to curve d). The Au-CNFs-1000 with high density of exposed AuNPs possesses higher specific surface area and active sites. It means that more AuNPs will take part in the reactions, leading to the relative higher electrocatalytic activity. The redox peak currents of HQ (curve d) are about 298.4 and 511.6 μA, with potentials at (-0.22 and 0.65 V), respectively. When the Au-CNFs were treated by a relative high heating rate (5 °C/min), the sizes of the AuNPs on CNFs increased from 5.8 to 10.2 nm and the redox peaks of HQ still exhibit a similar trend (Figure 11B). However, when the heating rate increased to 10 °C/min, Figure 11C indicate an inverse phenomena that the intensities of the redox peaks of HQ decreased with the graphitization temperature. The sizes of the AuNPs on CNFs increased from 10.7 to 23.5 nm and more serious aggregated AuNPs can be found, resulting in the weak electrochemical activity of AuNPs. The increased density of the AuNPs on CNFs cannot offset the decrease in the activities of AuNPs caused by the larger size and aggregation.

Therefore, relatively slower heating rates (2-5 °C/min) would lead to small increase in the sizes of AuNPs (below 10 nm) and the higher graphitization temperatures would bring about the higher exposed density of AuNPs on the surfaces of CNFs (600-1000 °C). The synergistic effects between the smaller size and higher exposed density of AuNPs lead to the increased electrochemical activity. Because of the highest electrochemical activity, we use the Au-CNFs-1000/GCE (2 °C/min) to evaluate the detection limits of the constructed biosensors. Figure 11D exhibits CV curves of Au-CNFs-1000 (2 °C/min) at different scan rates ranged from 20 to 300 mV s^{-1}. It is obvious that the shape of the CVs almost does not change in the range varied from 20 to 300 mV s^{-1} and the total peak current density increases with increasing potential scan rates, which demonstrates a good rate property and excellent electrochemical behavior for the Au-CNFs-1000 (2 °C/min) functionalized electrode. Meanwhile, the

inset in Figure 11B shows that there is a linear relationship between the redox peak current density and the scan rate for the electrode materials, indicating that the electrode process is a surface-controlled process.

For the amperometric sensing application, the Au-CNFs-1000 (2 °C/min) functionalized GCE electrodes are generally evaluated by measuring current response at a working potential of 0.0 V for the detection of H_2O_2. Figure 11E displays the amperometric response at the CNFs and the Au-CNFs-1000 (2 °C/min) modified GCE towards the successive addition of H_2O_2. As shown in Fig. S2, the CNFs/GCE exhibits a weaker response to the addition of H_2O_2, while the Au-CNFs/GCE shows a larger catalytic current to the changes of H_2O_2 concentration (Figure 11E). The rapid electrode response to the change of the H_2O_2 concentration could be attributed largely to the well-dispersed AuNPs immobilized on the Au-CNFs, which could effectively promote the electron transfer rate between the H_2O_2 and the electrode. With the continued addition of H_2O_2, the sensor responded rapidly to the substrates and could achieve 90% of the steady-state current within 3 s, indicating the fast amperometric response to the reduction of H_2O_2. Figure 11F shows a linear relationship with the concentration of H_2O_2 with the correlation coefficient of 0.997. The detection limit of 0.42 μM was estimated at a signal-to-noise ratio of 3.

Table 3 Summary of the response time, detection range, and detection time of as-prepared H_2O_2 electrochemical sensors in comparison with other reported sensors.

Electrochemical sensor	Response time (s)	Detecion range (μM)	Detecion limit (μM)	Ref
Au-CNFs	1	1-500	0.42	This work
HRP-AuNPs-PVA	1	1-500	0.5	58
HRP-AgNPs-PVA/PEI	2	5-550	2.5	30
HRP-Ag-PVA	2	10-560	5.6	31
HRP-Au NPs cellulose NFs	1	1-500	1	59
HRP-Fe_3O_4-silica	No data	2-24	0.43	60
HRP-sonogel-carbon	No data	4-100	1.6	61

Most of the biosensors for the detection of H_2O_2 should be assisted by immobilizing the horseradish peroxidase (HRP). In our present investigations, the constructed nonenzymatic sensors show lower detection limit and wider responding range for H_2O_2 without any enzyme. Table 3 summaries the response time, detection range, and detection time of as-prepared H_2O_2 electrochemical sensors in comparison with other reported sensors. It is can be clearly observed that our sensors without any enzyme exhibit lower detection limits and faster response than those systems with HRP as reported in literatures.

In addition, the Au-CNFs electrochemical sensors exhibit good reproducibility in the detection of H_2O_2 with a relative standard deviation (RSD) of about 3.3 % in the presence of 5.0 mM of H_2O_2 for more than 10 times measurements. The fabricated Au-CNFs electrodes used for 10 times were compared by the CV curves (Fig. S3) and the redox peaks are almost the same, indicating the excellent stability and reusability of electrochemical sensors. The sensors show lower detection limit and wider responding range, indicating that the fabricated sensor could be potentially used for monitoring the concentration of H_2O_2 without any enzyme.

Conclusions

A novel strategy for the design of novel nanostructures to show an unexpected behavior of AuNPs embedded in the interior of PANFs, which can emigrate to the external surfaces of the CNFs during the graphitization process have been demonstrated. With the conversion from the amorphous structures of PANFs to graphene layered structures of CNFs, the initial AuNPs embedded in the interior of the PANFs emigrate to the external surfaces of CNFs. The emigrations of AuNPs through the nanofiber matrix are strong depended on the graphitization temperature and heating rates. Three different heating rates at 2, 5, 10 °C/min and graphitization temperatures at 600, 800, 1000 °C, respectively, were performed to investigate the emigrations and the exposed density of AuNPs on the CNFs. In addition, the conversion in the chemical structures from C≡N structure to C=C-C=N structure during the graphitization process were investigated. The emigration phenomena of AuNPs are explained by an atom diffusion mechanism. These novel nanomaterials were constructed as a nonenzymatic H_2O_2 electrochemical sensor. The electrochemical sensors based on AuNPs with different density of exposed AuNPs exhibit significant promoted electrochemical activity with increased density of exposed AuNPs. The Au-CNFs with high density of exposed AuNPs possess higher specific surface area and active sites. It means that more AuNPs will take part in the reactions, leading to the relative higher electrocatalytic activity. The sensor showed lower detection limit and wider responding range, indicating that the fabricated sensor could be potentially used for monitoring the concentration of H_2O_2 without any enzyme. The present investigations provide a general route for the fabrication of nanostructures for novel electrochemical sensors, energy storage devices and so on.

Notes and references

1 X. Y. Lang, H. Y. Fu, C. Hou, G. F. Han, P. Yang, Y. B. Liu and Q. Jiang, *Nat. Comm.,* 2013, **4**, 2169-2156.
2 P. Lin and F.Yan, *Adv. Mater.,* 2012, **24**, 34-51.
3 C. Marichy, M. Bechelany and N. Pinna, *Adv. Mater.,* 2012, **24**, 1017-1032.
4 L. Matlock-Colangelo and A. J. Baeumner, *Lab Chip* 2012, **12**, 2612-2620.
5 Y. Q. Wang, B. Yan and L. X. Chen, *Chem. Rev.,* 2013, **113**, 1391-1428.

6 L. N. Cella, W. Chen, N. V. Myung and A. Mulchandani, *J. Am. Chem. Soc.,* 2010, **132**, 5024-5026.
7 X. M. Feng, R. M. Li, Y. W. Ma, R. F. Chen, N. E. Shi, Q. L. Fan and W. Huang, *Adv. Funct. Mater.,* 2011, **21**, 2989-2996.
8 Y. D. Jin, *Adv. Mater.,* 2012, **24**, 5153-5165.
9 S. Myung, A. Solanki, C. Kim, J. Park, K. S. Kim and K. B. Lee, *Adv. Mater.,* 2011, **23**, 2221-2225.
10 R. J. Chen, H. C. Choi, S. Bangsaruntip, E. Yenilmez, X. W. Tang, Q. Wang, Y. L. Chang, H. J. Dai, *J. Am. Chem. Soc.,* 2004, **126**, 1563-1568.
11 H. Im, X. J. Huang, B. Gu and Y. K. Choi, *Nat. Nanotech.,* 2007, **2**, 430-434.
12 Y. Xiang and Y. Lu, *Nat. Chem.,* 2011, **3**, 697-703.
13 N. J. Ronkainen, H. B. Halsall and W. R. Heineman, *Chem. Soc. Rev.,* 2010, **39**, 1747-1763.
14 J. Wang, *Chem. Rev.,* 2008, **108**, 814-825.
15 S. Mao, G. H. Lu, K. H. Yu, Z. Bo and J. H. Chen, *Adv. Mater.,* 2010, **22**, 3521-3526.
16 J. Lu, I. Do, L. T. Drzal, R. M. Worden and I. Lee, *ACS Nano,* 2008, **2**, 1825-1832.
17 A. L. Torre, M. D. C. Gimenez-Lopez, M. W. Fay, G. A. Rance, W. A. Solomonsz, T. W. Chamberlain, P. D. Brown and A. N. Khlobystov, *ACS Nano,* 2012, **6**, 2000-2007.
18 K. Besteman, J. O. Lee, F. G. M. Wiertz, H. A. Heering and C. Dekker, *Nano Lett.,* 2003, **3**, 727-730.
19 J. Wang, M. Musameh and Y. H. Lin, *J. Am. Chem. Soc.,* 2003, **125**, 2048-2049.
20 J. B. Mu, C. L. Shao, Z. C. Guo, Z. Y. Zhang, M. Y. Zhang, P. Zhang, B. Chen, Y. C. Liu, *ACS Appl. Mater. Interfaces,* 2011, **3**, 590-596.
21 A. Stein, Z. Y. Wang and M. A. Fierke, *Adv. Mater.,* 2009, **21**, 265-293.
22 X. W. Mao, F. Simeon, G. C. Rutledge and T. A. Hatton, *Adv. Mater.,* 2013, **25**, 1309-1314.
23 A. Greiner and J. H. Wendorff, *Angew. Chem. Int. Ed.,* 2007, **46**, 5670-5703.
24 L. W. Ji, O. Toprakci, M. Alcoutlabi, Y. F. Yao, Y. Li, S. Zhang, B. K. Guo, Z. Lin and X. W. Zhang, *ACS Appl. Mater. Interfaces,* 2012, **4**, 2672-2679.
25 X. F. Lu, X. J. Bian, G. D. Nie, C. C. Zhang, C. Wang and Y. Wei, *J. Mater. Chem.,* 2012, **22**, 12723-12730.
26 P. Q. Wang, D. Zhang, F. Y. Ma, Y. Ou, Q. N. Chen, S. H. Xie and J. Y. Li, *Nanoscale,* 2012, **4**, 7199-7204.
27 J. S. Bonso, G. D. Kalaw and J. P. Ferraris, *J. Mater. Chem. A,* 2014, **2**, 418-424.
28 M. R. Langille, M. L. Personick and C. A. Mirkin, *Angew. Chem. Int. Ed.,* 2013, **52**, 13910-13940.
29 A. S. Urban, X. S. Shen, Y. M. Wang, N. Large, H. Wang, M. W. Knight, P. Nordlander, H. Y. Chen and N. J. Halas, *Nano Lett.,* 2013, **13**, 4399-4403.
30 H. Zhu, M. L. Du, M. Zhang, P. Wang, S. Y. Bao, L. N. Wang, Y. Q. Fu and J. M. Yao, *Biosens. Bioelectron.,* 2013, **49**, 210-215.
31 H. Zhu, M. L. Du, M. Zhang, P. Wang, S. Y. Bao, Y. Q. Fu and J. M. Yao, *Sensor. Acturat. B-Chem.,* 2013, **185**, 608-619
32 H. Zhu, M. Zhang, S. Y. Cai, Y. T. Cai, P. Wang, S. Y. Bao, M. L. Zou and M. L. Du, *RSC Adv.,* 2014, **4**, 794-804.
33 H. Zhu, M. L. Du, M. Zhang, P. Wang, S. Y. Bao, M. L. Zou, Y. Q. Fu and J. M. Yao, *Biosens. Bioelectron.,* 2014, **54**, 91-101.
34 J. Li, S. B. Tang, L. Lu and H. C. Zeng, *J. Am. Chem. Soc.,* 2007, 129, 9401-9409.
35 I. Kvande, J. Zhu, T. J. Zhao, N. Hammer, M. Ronning, S. Raaen, J. C. Walmsley and D. Chen, *J. Phys. Chem. C,* 2010, **114**, 1752-1762.
36 D. Y. Shin, B. Jeong, B. S. Mun, H. Jeon, H. J. Shin, J. Baik and J. Lee, *J. Phys. Chem. C,* 2013, **117**, 11619-11624.
37 S. Hermans, V. Bruyr and M. A. Devillers, *J. Mater. Chem.,* 2012, **22**, 14479-14486.
38 C. H. Liang, W. Xia, M. V. D. Berg, Y. M. Wang, H. Soltani-Ahmadi, O. Schluter, R. A. Fischer and M. Muhler, *Chem. Mater.,* 2009, **21**, 2360-2366.
39 Z. X. Yang, G. D. Du, Z. P. Guo, X. B. Yu, S. Li, Z. X. Chen, P. Zhang and H. K. Liu, *Nanoscale,* 2010, **2**, 1011-1017.
40 H. Q. Hou and D. H. Reneker, *Adv. Mater.,* 2004, **16**, 69-73.
41 H. Zhu, M. L. Du, M. L. Zou, C. S. Xu, N. Li and Y. Q. Fu, *J. Mater. Chem.,* 2012, **22**, 9301-9307.
42 M. L. Zou, M. L. Du, H. Zhu, C. S. Xu, N. Li and Y. Q. Fu, *Polym. Eng. Sci.,* 2013, **53**, 1099-1108.
43 L. J. Wang, J. H. Hu, H. Y. Zhang and T. Zhang, *Chem. Commun.,* 2011, **47**, 6837-6839.
44 C. Y. Su, Y. F. Tong, M. Y. Zhang, Y. Zhang and C. L. Shao, *RSC Adv.,* 2013, **3**, 7503-7512.
45 Y. Aykut, *ACS Appl. Mater. Interfaces,* 2012, **4**, 3405-3415.
46 B. S. Lee, S. B. Son, K. M. Park, G. S. Lee, K. H. Oh, S. H. Lee and W. R. Yu, *ACS Appl. Mater. Interfaces,* 2012, **4**, 6702-6710.
47 Z. C. Xu, Y. L. Hou and S. H. Sun, *J. Am. Chem. Soc.,* 2007, **129**, 8698-8699.
48 H. Zhu, M. L. Du, D. L. Yu, Y. Wang, L. N. Wang, M. L. Zou, M. Zhang and Y. Q. Fu, *J. Mater. Chem. A,* 2013, **1**, 919-929.
49 Y. Negishi, K. Nobusada and T. Tsukuda, *J. Am. Chem. Soc.,* 2005, **127**, 5261-5270.
50 A. Tanaka, Y. Takeda, M. Imamura and S. Sato, *Phys. Rev. B,* 2003, **68**, 195415.
51 W. Li, L. S. Zhang, Q. Wang, Y. Yu, Z. Chen, C. Y. Cao, W. G. Song, *J. Mater. Chem.,* 2012, **22**, 15342-15347.
52 J. Q. Wang, K. Pan, E. P. Giannelis and B. Cao, *RSC Adv.,* 2013, **3**, 8978-8987.
53 A. G. El-Deen, N. A. M. Barakat, K. A. Khalil and H. Y. Kim, *J. Mater. Chem. A,* 2013, **1**, 11001-11010.
54 M. Zhang, E. Uchaker, S. Hu, Q. F. Zhang, T. H. Wang, G. Z. Cao and J. Y. Li, *Nanoscale,* 2013, **5**, 12342-12349.
55 J. N. Wang, W. Qin, X. Q. Liu and H. Q. Liu, *RSC Adv.,* 2013, **3**, 11132-11139.
56 W. B. Li, Z. H. Yang, G. L. Zhang and Q. Meng, *Ind. Eng. Chem. Res.,* 2013, **52**, 6492-6501.
57 K. K. Nanda, S. N. Sahu and S. N. Behera, *Phys. Rev. A,* 2002, **66**, 013208.
58 J. Wang, H. B. Yao, D. He, C. L. Zhang and S. H. Yu, *ACS Appl. Mater. Interfaces,* 2012, **4**, 1963-1971.
59 T. Zhang, W. Wang, D. Zhang, X. Zhang, Y. Ma, Y. Zhou and L. Qi, *Adv. Funct. Mater.,* 2010, **20**, 1152-1160.
60 Y. H. Won, D. Aboagye, H. S. Jang, A. Jitianu, L. A. Stanciu, *J. Mater. Chem.,* 2010, **20**, 5030-5034.
61 J. L. H. H. de Cisneros, M. Elkaoutit, I. Naranjo-Rodriguez, M. Dominguez, M. P. Hernandez-Artiga and D. Bellida-Milla, *Electrochim. Acta,* 2008, **53**, 7131-7137.